PAPER

Check for updates

Photo-electrochemical hydrogen production from neutral phosphate buffer and seawater using micro-structured p-Si photo-electrodes functionalized by solution-based methods†

Anurag Kawde, [ID] [ab] Alagappan Annamalai, [ID] [c] Lucia Amidani,[b] Manuel Boniolo,[d] Wai Ling Kwong, [ID] [d] Anita Sellstedt,[e] Pieter Glatzel,[b] Thomas Wågberg[c] and Johannes Messinger [ID] *[ad]

Solar fuels such as H_2 generated from sunlight and seawater using earth-abundant materials are expected to be a crucial component of a next generation renewable energy mix. We herein report a systematic analysis of the photo-electrochemical performance of TiO_2 coated, microstructured p-Si photo-electrodes (p-Si/TiO_2) that were functionalized with CoO_x and NiO_x for H_2 generation. These photocathodes were synthesized from commercial p-Si wafers employing wet chemical methods. In neutral phosphate buffer and standard 1 sun illumination, the p-Si/TiO_2/NiO_x photoelectrode showed a photocurrent density of -1.48 mA cm^{-2} at zero bias (0 V_{RHE}), which was three times and 15 times better than the photocurrent densities of p-Si/TiO_2/CoO_x and p-Si/TiO_2, respectively. No decline in activity was observed over a five hour test period, yielding a Faradaic efficiency of 96% for H_2 production. Based on the electrochemical characterizations and the high energy resolution fluorescence detected X-ray absorption near edge structure (HERFD-XANES) and emission spectroscopy measurements performed at the Ti Kα_1 fluorescence line, the superior performance of the p-Si/TiO_2/NiO_x photoelectrode was attributed to improved charge transfer properties induced by the NiO_x coating on the protective TiO_2 layer, in combination with a higher catalytic activity of NiO_x for H_2-evolution. Moreover, we report here an excellent photo-electrochemical performance of p-Si/TiO_2/NiO_x photoelectrode in corrosive artificial seawater (pH 8.4) with an unprecedented photocurrent density of 10 mA cm^{-2} at an applied potential of -0.7 V_{RHE}, and of 20 mA cm^{-2} at -0.9 V_{RHE}. The applied bias photon-to-current conversion efficiency (ABPE) at -0.7 V_{RHE} and 10 mA cm^{-2} was found to be 5.1%.

Introduction

The CO_2 released by burning fossil fuels for transportation, production of electricity and heating is a major contributor to global warming.[1–3] In order to limit the greenhouse effect, it is necessary to replace fossil fuels with renewable and carbon-neutral or 'green' fuels.[1] On Earth's surface, sunlight is the most abundant source of free energy, and seawater can provide a plentiful supply of electrons and protons as ingredients for

[a]Umeå University, Department of Chemistry, Sweden. E-mail: johannes.messinger@kemi.uu.se

[b]European Synchrotron Radiation Facility (ESRF), Grenoble, France

[c]Umea University, Department of Physics, Sweden

[d]Molecular Biomimetics, Department of Chemistry – Ångström Laboratory, Uppsala University, Sweden

[e]Umeå University, Department of Plant Physiology, Umeå Plant Science Centre (UPSC), Umeå, Sweden

† Electronic supplementary information (ESI) available. See DOI: 10.1039/c8se00291f

making solar fuels.[4–8] Natural photosynthesis and recent lab-scale artificial photosynthesis devices have demonstrated high efficiencies in solar-driven water splitting into molecular hydrogen and oxygen.[9–12] However, enabling global-scale solar-fuel generation requires the fabrication of devices, in particularly of photoelectrodes, from earth-abundant materials. To obtain the maximal device performance, the interplay between light-harvesting, charge separation and electron/proton transport, as well as water oxidation and reduction catalysis needs to be carefully optimized[2,3,12–20]

The intrinsic band gap (1.1 eV) of silicon photo-electrodes make them capable of absorbing a broad spectrum of the solar light. Over the past decades, they have thus gathered much attention towards photo-electrochemical (PEC) water splitting.[21–26] The band structure of n-type Si promotes the photo-anodic oxygen evolution reaction (OER),[27,28] while p-type Si facilitates the photo-cathodic hydrogen evolution reaction (HER).[22] However, the difference between the potentials of the valence band edge of p-Si and that of the H^+/H_2 redox couple is

relatively small which limits the photo-voltage and leads to slow HER kinetics.[29] The surface area of the Si photo-electrodes can be significantly increased *via* nano or micro structuring.[30] This not only increases light absorption of Si but also improves HER kinetics by shortening charge carrier transport pathways.[24,31]

When Si is placed in an aqueous environment, it forms an insulating oxide layer, which significantly reduces its HER efficiency.[32] In addition, Si is only stable at strongly acidic[33] and alkaline[34] pH if protected. Both processes can be suppressed highly efficiently by applying a thin TiO_2 over coating.[35–37] In most studies the fabrication of the TiO_2 protective layer involves the use of relatively expensive high vacuum technology such as atomic layer deposition (ALD).[34,38–40] While ALD is used industrially for applying thin metal layers during the production of electronic components for computers and other electronic devices, it may still be useful to explore cheap and scalable wet-chemical methods for producing large areas of coatings of 20–50 nm thickness.[41,42] The performance of Si/TiO_2 photo-electrodes can be improved by decoration with suitable co-catalysts.[38,43] Decoration with NiO_x has been studied for improving OER catalysis,[27,44,45] but there are only a few studies on the application of NiO_x as HER catalysts at neutral (or near neutral) pH.[46–49] To the best of our knowledge, NiO_x has not yet been studied as HER co-catalyst on the surface of p-Si/TiO_2 for photoelectrochemical seawater reduction to H_2.

Herein, we report the fabrication of efficient HER photo-electrodes consisting of CoO_x or NiO_x decorated p-Si/TiO_2. The photo-electrodes were prepared by micro-structuring commercial p-Si wafers using a well-documented electroless wet etching technique.[50,51] The resulting microwire surface was coated with a protective TiO_2 layer and subsequently functionalized with CoO_x or NiO_x co-catalysts using simple solution-based techniques. The electrodes obtained by the various fabrication steps were systematically studied, and the photo-electrochemical responses of the final p-Si/TiO_2/NiO_x and p-Si/TiO_2/CoO_x electrodes were measured in neutral pH phosphate buffer and in artificial seawater at pH 8.4. The PEC performance of functionalized p-Si photoelectrodes were also studied without a TiO_2 layer to establish the effect of TiO_2 as efficient charge separation layer between p-Si and the co-catalysts. Detailed electrochemical and X-ray spectroscopic studies were performed to elucidate the origin of the significantly better performance of p-Si/TiO_2/NiO_x as compared to p-Si/TiO_2/CoO_x.

Results and discussion

Preparation and structural characterization of HER photo-electrodes

The experimental steps involved in the synthesis of our p-Si photo-electrodes are summarized schematically in Fig. 1 (see ESI† for experimental methods). After a reductive cleaning of the commercial p-Si wafers to remove the surface SiO_2, wet etching was employed to obtain high-aspect ratio micro-structured p-Si electrodes.[50,51] These 'as-synthesized' p-Si photo-electrodes (Fig. 2(a) and (b)) were subsequently spin-coated in two steps, first with a TiO_2 sol and subsequently with either a NiO_x or CoO_x sol. Each spin-coating step was followed by drying at room temperature and calcination at 380 °C. The scanning electron microscopy (SEM) top and side views of the as-synthesized p-Si (Fig. 2(a) and (b)) show the microstructure morphology. Fig. 2(c)–(f) show that the sol–gel method in combination with spin coating resulted in the formation of a protective TiO_2 overcoating and a co-catalysts film that fully covers the p-Si. The energy dispersive X-ray spectroscopy (EDX) cross-sections of the functionalized p-Si photo-electrodes are
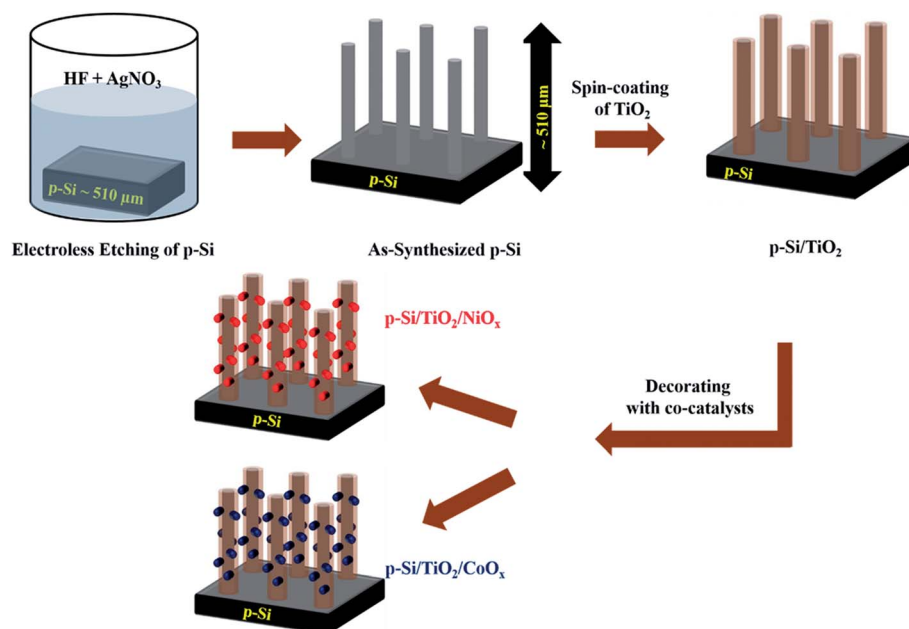

Fig. 1 Schematic representation (not to scale) of the preparation steps of p-Si micro-wires by wet-etching, their coating with TiO_2 and subsequent functionalization with NiO_x or CoO_x *via* spin coating and sintering. The procedure is described in detail in the ESI.†
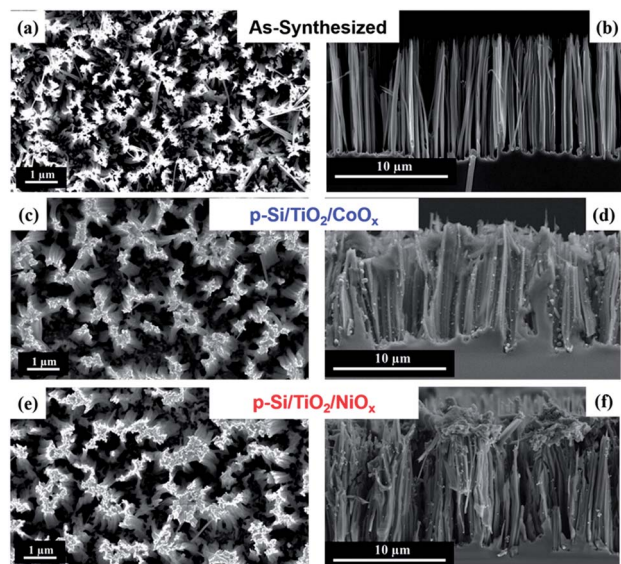
Fig. 2 SEM Images showing the planar top views (a), (c) and (e) and the cross-sectional view (b), (d) and (f), of as-synthesized and functionalized p-Si.

shown in ESI Fig. S1–S3.† On the basis of the SEM and TEM data shown in ESI Fig. S4† we conservatively estimate that the TiO_2 layer has a thickness ranging between 20–50 nm. The elemental composition and the presence of CoO_x and NiO_x were confirmed using XPS, for details see ESI Fig. S5.†

Photo-electrochemical characterization of the HER electrodes in neutral phosphate buffer

The photo-electrochemical performances of the p-Si photo-electrodes obtained after each preparation step were carefully studied at 1 sun illumination in neutral phosphate buffer. The linear sweep voltammogram (LSV) traces in Fig. 3a show that the photocurrent density of untreated planar p-Si stays negligible over the entire potential range studied (dark currents are shown in ESI Fig. S6†). The slightly higher photocurrent performance of the as-synthesized, micro-structured p-Si photoelectrode (purple trace, Fig. 3a) as compared to planar p-Si (green trace, Fig. 3a) is in line with an earlier report[34] and can be explained by the better light absorption and charge transport owing to the one dimensional morphology and improved surface area. This advantage of micro-structuring[52] is even more obvious for the fully functionalized photo-electrodes as shown in Fig. 3b (LSVs for planar Si and planar Si/TiO_2 are shown in Fig. S7†). Coverage of microstructured p-Si with a protective TiO_2 layer leads to a further minor increase in the photocurrent (black trace in Fig. 3a), likely due to the absence of an insulating Si-oxide surface layer and/or the better catalytic HER performance of TiO_2 vs. p-Si. The nearly 6-fold increase in photocurrent after functionalization with CoO_x ($J = -0.50$ mA cm^{-2}@0 V_{RHE}) and the 15-fold increase in case of NiO_x ($J = -1.40$ mA cm^{-2}@0 V_{RHE}) shows that the photo-charge carriers of our control sample ($J = -0.09$ mA cm^{-2}@0 V_{RHE}) can be used much more efficiently for proton reduction if suitable co-catalysts are provided (blue and red traces in Fig. 3a). Interestingly, Fig. 3c
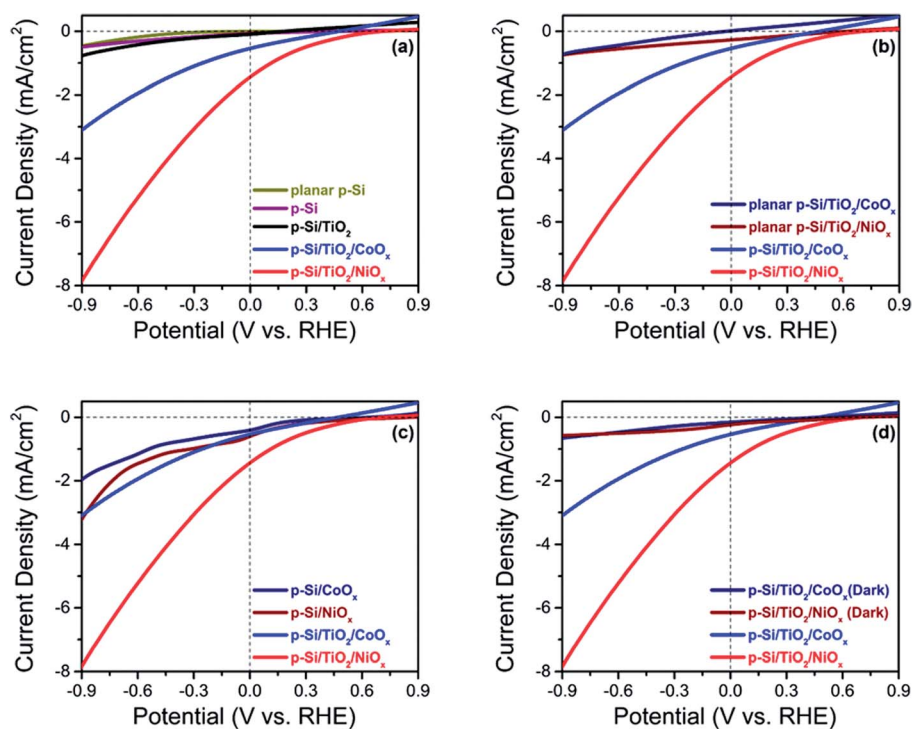

Fig. 3 Linear sweep voltammograms recorded under 1 sun illumination in potassium phosphate buffer (0.2 M; pH 7.00) (a) planar p-Si, a surface etched p-Si with microwires (p-Si), and functionalized p-Si photo-electrodes (b) fully functionalized planar Si and functionalized p-Si (c) functionalized p-Si with and without the intermittent TiO_2 layer (d) functionalized p-Si in dark and in illumination.

shows that the current densities obtained are much smaller in absence of the intermittent TiO_2 layer, indicating that function of the TiO_2 layer goes far beyond a simple protective function. The magnitude of the photo current is illustrated for the fully assembled photo-electrodes in Fig. 3d by comparing the corresponding light and dark traces.

The same trends as for the photo currents are also seen in the respective onset potentials (V_{onset}) for H_2-evolution, here defined as the potential needed for reaching a net photocurrent density of -0.1 mA cm^{-2}.[53] A positive (anodic) shift of the onset potential (V_{onset}) was observed for the co-catalyst functionalized electrodes as compared to as-synthesized and p-Si/TiO_2: the V_{onset} of the control p-Si/TiO_2 sample was observed at -0.66 V$_{RHE}$, whereas those for p-Si/TiO_2/CoO_x and p-Si/TiO_2/NiO_x were shifted to $+0.27$ V$_{RHE}$ and $+0.42$ V$_{RHE}$, respectively (ESI Table S1†). The V_{onset} value for our p-Si/TiO_2/NiO_x photoelectrode is remarkable when compared to a recent report by Zhang and coworkers,[33] where a $V_{onset} = +0.25$ V$_{RHE}$ ($J = -0.1$ mA cm^{-2}) was obtained for p-Si/$NiCoSe_x$ nanopillars in 0.5 M H_2SO_4 where the concentration of protons is 10^6 times higher as compared to the neutral pH electrolyte employed here.[33,43] The excellent performance of NiO_x at neutral pH condition, which is further manifested by the detailed comparison to further co-catalysts functionalized p-Si based photo-electrodes reported in the literature (ESI Table S1†), may be attributed either to an intrinsically better HER performance of NiO_x compared to CoO_x, and/or to a superior charge transfer between p-Si and the NiO_x via the protective TiO_2 underlayer. This will be analysed in subsequent sections.

Photochemical H_2 generation in neutral phosphate buffer

The photo-generation of H_2 was measured using gas chromatography (GC) at a constant potential of 0 V$_{RHE}$. Fig. 4a shows the results for p-Si/TiO_2/CoO_x (blue) and p-Si/TiO_2/NiO_x (red). Over a period of 5 hours of continuous illumination, a near linear production of H_2 was observed yielding ~128 μmol cm^{-2} and ~44 μmol cm^{-2} of H_2 for p-Si/TiO_2/NiO_x and p-Si/TiO_2/CoO_x respectively. The simultaneously recorded photocurrent density (Fig. 4b) was essentially stable at -1.48 mA cm^{-2} (p-Si/TiO_2/NiO_x) and -0.48 mA cm^{-2} (p-Si/TiO_2/CoO_x) over the five hours of the measurements, indicating a total lifetime extending by far the chosen duration of this experiment. XES scans taken after these experiments demonstrate that Pt from the counter electrode was not deposited onto our working electrodes during these experiments (ESI Fig. S8†). This results in a Faradaic efficiency of 96% (p-Si/TiO_2/NiO_x) and 93% (p-Si/TiO_2/CoO_x) and in applied bias photon to current conversion efficiencies (ABPE) of 1.74% for p-Si/TiO_2/NiO_x and 0.54% for p-Si/TiO_2/CoO_x at 0 V$_{RHE}$. The excellent performance of NiO_x may in part also be attributed to its conversion into $Ni(OH)_2$ upon contact with water.[48,49,54] $Ni(OH)_2$ formation is in agreement with the XPS spectra taken after the 5 hour performance test (ESI Fig. S5†). While we cannot exclude that a transient light-induced formation of NiOOH contributes to the excellent performance of NiO_x, as suggested recently for NiO_x nanoparticles,[54] we do not observe a stable NiOOH formation in the above mentioned XPS spectra, as expected under negative bias.
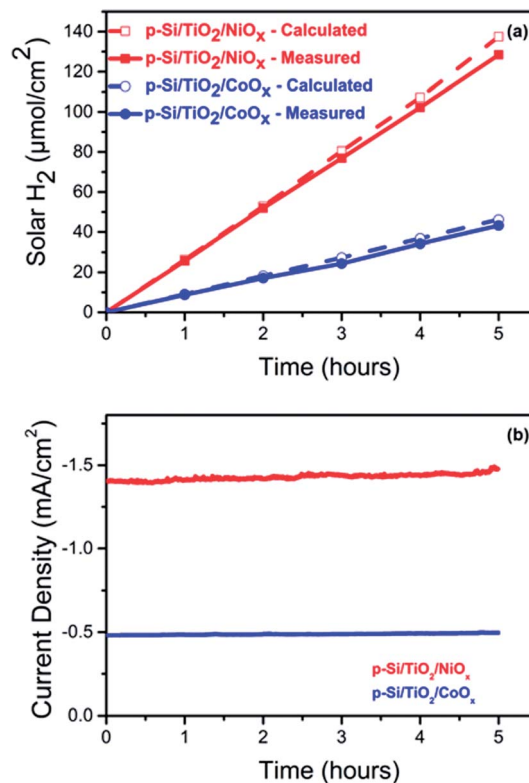

Fig. 4 Comparison of (a) the calculated and measured solar hydrogen production per geometric surface area of the photoelectrode and (b) of the current density of NiO_x (red) and CoO_x (blue) functionalized p-Si photo-electrodes over 5 hours of continuous operation. The data displayed in (a) and (b) were obtained simultaneously at 0.0 V$_{RHE}$ and 1 sun illumination.

Charge transport kinetics

To understand the differences between the photoelectrochemical performance of non-functionalized and NiO_x- or CoO_x-functionalized p-Si/TiO_2 photo-electrodes, the transport of photoelectrons generated in p-Si to the surface and further to the protons in the phosphate buffer (pH 7.0) were studied by using electrochemical impedance spectroscopy (EIS). The Nyquist plots of the EIS data measured at 1 sun illumination are shown in Fig. 5 along with the equivalent circuit diagram employed for their analysis. The smaller semi-circle (high frequency region) corresponds to the resistance for the charge transfer from p-Si through TiO_2 to the surface (R_{CT1}, CPE$_1$), whereas the larger semicircle (low frequency region) corresponds to the photoelectrode/electrolyte interfacial charge transfer resistance described by R_{CT2} and CPE$_2$. The data in Fig. 5 and ESI Table S2† show that the charge transport resistance for both processes is smallest for NiO_x, and increases for p-Si/TiO_2/CoO_x and is largest for the non-functionalized p-Si/TiO_2. R_{CT1} increases from 807 Ω to 1672 Ω and 1763 Ω, while R_{CT2} from 2519 Ω to 6646 Ω and 29 840 Ω. The effective R_s also increases in the same order, indicating that p-Si/TiO_2/NiO_x has the best charge transfer kinetics.[55]

To further investigate the electronic and interfacial properties, the flat band potential (V_{FB}) and the carrier concentration
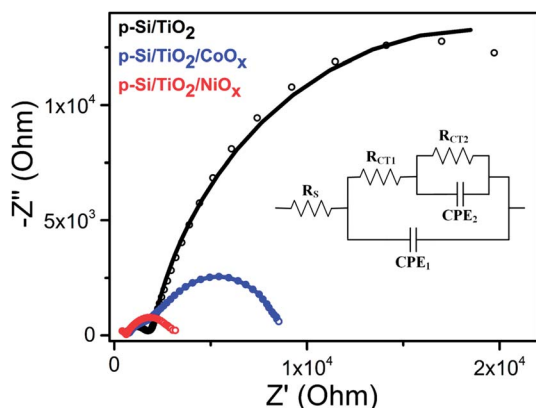
Fig. 5 Nyquist plots of p-Si/TiO$_2$ (black), p-Si/TiO$_2$/CoO$_x$ (blue), p-Si/TiO$_2$/NiO$_x$ (red) measured at 0.0 V$_{RHE}$ under 1 sun illumination. The inset shows the equivalent circuit employed for analyzing the Nyquist plots. The fit data are provided in ESI Table S2.†

(N_D) were studied by Mott–Schottky measurements. Fig. 6(a–c) show that all photo-electrodes display a negative slope in the Mott–Schottky plots, consistent with the p-type doping of the Si substrate. The carrier concentrations (N_D) of the photo-electrodes were calculated from the slopes of Mott–Schottky plots, yielding values of 1.52×10^{14} cm^{-3}, 1.98×10^{15} cm^{-3} and 3.73×10^{15} cm^{-3} for p-Si/TiO$_2$ and CoO$_x$ or NiO$_x$ functionalized photo-electrodes, respectively. Thus, both CoO$_x$ and NiO$_x$ functionalized photo-electrodes show one-order higher donor densities compared to the p-Si/TiO$_2$ control sample. This is in line with the observed H$_2$ generation rates at neutral pH, as well as with the order of the current densities and the charge transfer properties described above.

By fitting the linear regions (minimum range of 200 mV)[56] of the Mott–Schottky plots and extrapolating the line to the X-axis, the flat band potential V_{FB} can be deduced. Significant differences were observed: the V_{FB} of the Si/TiO$_2$ control sample was 0.63 V$_{RHE}$, whereas V_{FB} of the CoO$_x$ and NiO$_x$ modified photo-electrodes were 0.68 V$_{RHE}$ and 0.79 V$_{RHE}$, respectively. The anodic shifts of 0.05 V and 0.16 V compared to the control indicate that p-Si/TiO$_2$/NiO$_x$ has the least recombination losses,[57] suggesting that NiO$_x$ passivates the surface defects more efficiently than CoO$_x$. The more positive anodic shifts of the V_{FB}

for the p-Si/TiO$_2$/NiO$_x$ may be attributed to dissipation of potential drop at the Helmholtz layer and space charge region at the p-Si/TiO$_2$/NiO$_x$ – electrolyte interface.[45] An anodically shifted V_{FB} enhances the HER kinetics by lowering the potential for transporting electrons to the surface.[46,58–62]

Effects of co-catalysts on the local geometry of TiO$_2$

The electrochemical characterization of our photo-electrodes shows that the charge transfer properties of the interfacial TiO$_2$ layer are improved to various degrees by applying the CoO$_x$ or NiO$_x$ co-catalyst layers and sintering at 380 °C for two hours, indicating a modification of the TiO$_2$ coating by this procedure. In addition, the significant and different performance increases of p-Si/CoO$_x$ vs. p-Si/TiO$_2$/CoO$_x$ and p-Si/NiO$_x$ vs. p-Si/TiO$_2$/NiO$_x$ indicate an important role of the TiO$_2$ layer for the overall performance of the photo-electrodes. Thus, K-edge HERFD-XANES measurements were performed at the Ti K-edge (Fig. 7a and b) to elucidate changes in the atomic and electronic structure of TiO$_2$ induced by co-catalyst decoration. A schematic view of the optics and the experimental set up is presented elsewhere.[63,64] The pre-edge region of the XAS spectra (4967 to 4976 eV) is particularly sensitive to the symmetry at the Ti sites.[65,66] The pre-edge of crystalline TiO$_2$ has three characteristic peaks, denoted as A1, A2 and A3.[67] The pre-edge peaks A2 and A3 mainly arise from dipolar transitions from the Ti 1s shell and are thus affected by p–d mixing,[66,68] which in turn depends on the local bonding geometry. In contrast, the quadrupolar 1s to 3d transition gives rise to A1 and the low energy shoulder in A2.[69,70] Thus the number and position of the peaks in the pre-edge region contain information about the local coordination of Ti in TiO$_2$.[67] In anatase and amorphous TiO$_2$, the intensity of this shoulder is particularly sensitive to the presence of low coordination Ti sites as demonstrated by investigations of TiO$_2$ nanoparticles.[71,72] Additional structural information can be obtained from the spectral shape of the post-edge region (B and C in Fig. 7a), which derives from the excitation of a 1s electron to one of the unoccupied states with p-symmetry with respect to Ti. Such transitions are highly sensitive to the local structure around the absorber.[67]

Fig. 7a shows the HERFD-XANES spectra of p-Si/TiO$_2$, p-Si/TiO$_2$/CoO$_x$, and p-Si/TiO$_2$/NiO$_x$, while the reference spectra of
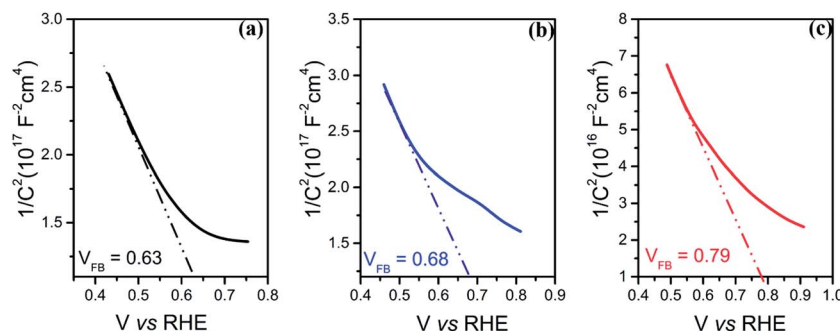

Fig. 6 Mott–Schottky measurements of (a) p-Si/TiO$_2$ (b) p-Si/TiO$_2$/CoO$_x$ and (c) p-Si/TiO$_2$/NiO$_x$.
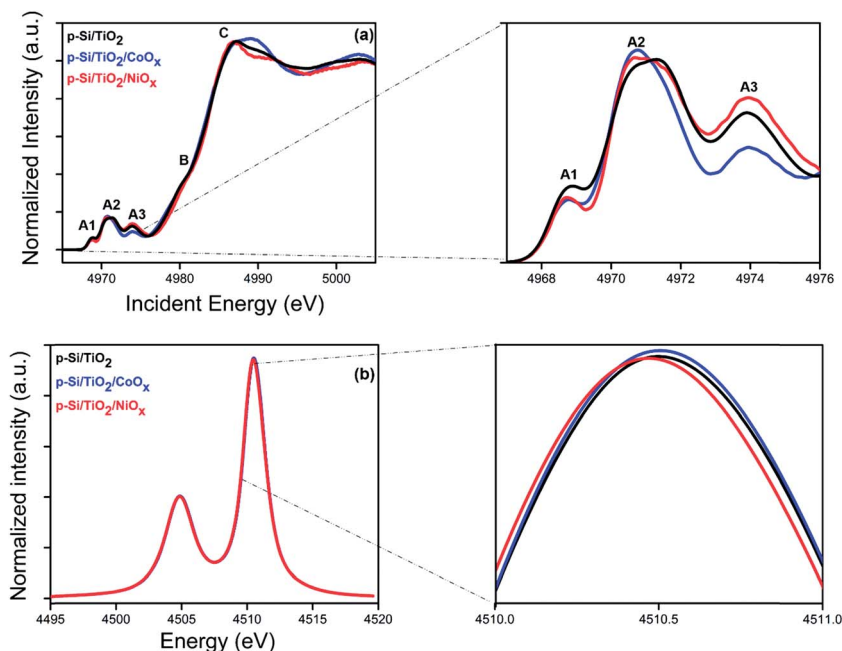
Fig. 7 X-ray spectroscopy characterization of p-Si/TiO$_2$ (black), p-Si/TiO$_2$/CoO$_x$ (blue), p-Si/TiO$_2$/NiO$_x$ (red): (a) HERFD-XANES spectra acquired at the Ti K-edge. The magnified view on the right shows the pre-edge peaks. (b) Kα emission lines. The magnified view on the right shows the Kα peak maximum.

TiO$_2$ anatase, TiO$_2$ rutile, and sol–gel processed protective TiO$_2$ are displayed in ESI Fig. S9.† The overall spectral shape with three strong pre-edge features is preserved in all three samples. Together with the largely invariant Kα lines (Fig. 7b) this finding confirms that the crystallinity of the protective TiO$_2$ layer remains unchanged, *i.e.* that in all cases Ti is in oxidation state +IV with a six-fold coordination. However, a detailed comparison revealed clear spectral differences between the pre-edge peaks of the three samples that are indicative of variously distorted TiO$_2$ octahedra. In addition, the absorption peak C is also different for all the samples.[71] The precise nature of these changes could possibly be addressed using computational modeling, which is beyond the scope of this study. Nevertheless, the present data demonstrate that an intricate interplay between all components of the photo-electrode, including the TiO$_2$ layer, exists that contributes to the overall catalytic performance.

Functional characterisation of HER activity in artificial seawater (pH 8.4)

Because of the vast seawater resources on Earth, we tested also the photo-catalytic performance of our best electrode, p-Si/TiO$_2$/NiO$_x$, in artificial seawater. Fig. 8 displays the photo-electrochemical performance of p-Si/TiO$_2$/NiO$_x$ in neutral phosphate electrolyte and artificial seawater (pH 8.4). A shift of V_{onset} by −0.12 V$_{\text{RHE}}$ is observed for artificial seawater compared to neutral phosphate buffer. This cathodic shift is expected due to the lower proton concentration at the higher pH. However, despite the less favourable onset potential, the p-Si/TiO$_2$/NiO$_x$ photoelectrode was highly efficient in H$_2$

generation at increasing potentials. A photocurrent density of 10 mA cm^{-2} was achieved at 1 sun illumination and an applied potential of −0.7 V$_{\text{RHE}}$, and 20 mA cm^{-2} at about −0.9 V$_{\text{RHE}}$.

To the best of our knowledge, there are only a small number of studies describing the photo-electrochemical hydrogen generation by seawater splitting.[4,6–8] In a recent study, Mase *et al.*[73] reported the photocatalytic production of hydrogen peroxide (H$_2$O$_2$) from seawater at pH 1.3 with a solar-to-electricity efficiency of 0.28%, and a photocatalytic production efficiency of H$_2$O$_2$ of 0.55%. Ji *et al.*[6] found that their NiO/Ni/La$_2$Ti$_2$O$_7$ photo catalysts were suitable for solar hydrogen generation from both natural and artificial seawater, but that Mg^{2+} and Ca^{2+} reduce the rate of H$_2$-evolution. Fig. 8(b) and (c) show that our photoelectrode when operated in artificial seawater at an applied potential of −0.3 V$_{\text{RHE}}$ and 1 sun illumination, produces H$_2$ at a nearly constant rate of about −1.5 mA cm^{-2} over 8 hours. The possibility of photo-oxidation of Cl$^-$ to Cl$_2$ has been discussed for the photo-electrochemical seawater splitting[4,7] however, we did not detect chlorine gas formation employing gas chromatography. The ABPE in the seawater splitting was calculated to be 1.26% at −0.3 V$_{\text{RHE}}$, which corresponds to a current density of −1.5 mA cm^{-2}, after 8 hours of illumination with a Faradaic efficiency close to 91%, further indicating that Cl$^-$ oxidation and Mg^{2+}/Ca^{2+} deposition are at best minor side reactions. Importantly, an ABPE of 5.1% was observed at −0.7 V$_{\text{RHE}}$. These surprisingly good results highlight the importance of the TiO$_2$ layer in combination with NiO$_x$ as an efficient HER catalysts, which can likely be further optimized in future for even more efficient solar seawater splitting.
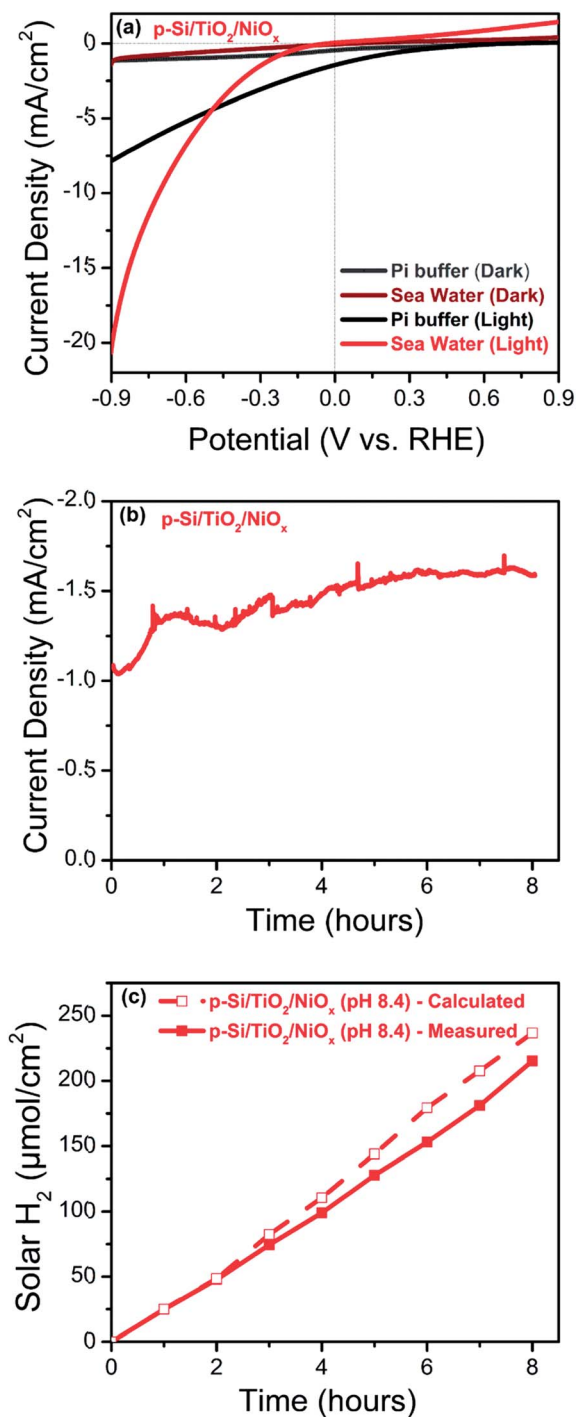
Fig. 8 Photo-electrochemical performance of the p-Si/TiO$_2$/NiO$_x$ photoelectrode recorded under 1 sun illumination in artificial seawater at pH 8.4 (red) or pH 7.0 (black; 0.2 M phosphate buffer): (a) linear sweep voltammograms, (b) photo-current density measured at −0.3 V$_{RHE}$ and (c) comparison of calculated (open squares) and measured (closed squares) photo generated hydrogen per geometric surface area of the photo-electrode at −0.3 V$_{RHE}$ and 1 sun.

Conclusions

We demonstrate here a simple solution-based approach for the synthesis of photo-electrodes with earth abundant materials.

The photo-electrodes presented in this study can harvest solar energy and utilize it for splitting corrosive seawater, making it an attractive system for large-scale application. Our finding of sustained H$_2$ evolution with >1.2% ABPE in artificial seawater using a p-Si/TiO$_2$/NiO$_x$ at a bias of −0.3 V$_{RHE}$ is highly encouraging, but further significant improvements to optimize the presented photo-electrodes are needed before practical applications become feasible. Importantly, the dual effect of NiO$_x$, on the charge transfer through the protective TiO$_2$ layer and for HER catalysis, points towards new ways for photoelectrode manufacturing.

Conflicts of interest

The authors declare no conflict of interest.

Acknowledgements

References

1 N. S. Lewis and D. G. Nocera, *Proc. Natl. Acad. Sci. U. S. A.*, 2006, **103**, 15729–15735.
2 M. Grätzel, *Nature*, 2001, **414**, 338.
3 T. Faunce, S. Styring, M. R. Wasielewski, G. W. Brudvig, A. W. Rutherford, J. Messinger, A. F. Lee, C. L. Hill, M. Fontecave and D. R. MacFarlane, *Energy Environ. Sci.*, 2013, **6**, 1074–1076.
4 W. Luo, Z. Yang, Z. Li, J. Zhang, J. Liu, Z. Zhao, Z. Wang, S. Yan, T. Yu and Z. Zou, *Energy Environ. Sci.*, 2011, **4**, 4046–4051.
5 J. Augustynski, R. Solarska, H. Hagemann and C. Santato, *Proc. SPIE*, 2006, **6340**, U140–U148.
6 S. M. Ji, H. Jun, J. S. Jang, H. C. Son, P. H. Borse and J. S. Lee, *J. Photochem. Photobiol., A*, 2007, **189**, 141–144.
7 X. Guan, F. A. Chowdhury, N. Pant, L. Guo, L. Vayssieres and Z. Mi, *J. Phys. Chem. C*, 2018, **125**, 13797–13802.
8 L. Zhang, I. Álvarez-Martos, A. Vakurov and E. E. Ferapontova, *Sustainable Energy Fuels*, 2017, **1**, 842–850.
9 K. Sivula, F. Le Formal and M. Grätzel, *ChemSusChem*, 2011, **4**, 432–449.
10 T. F. Jaramillo, K. P. Jørgensen, J. Bonde, J. H. Nielsen, S. Horch and I. Chorkendorff, *Science*, 2007, **317**, 100–102.
11 A. Fujishima and K. Honda, *Nature*, 1972, **238**, 37.
12 B. Wang, J. Zhang and F. Huang, *Appl. Surf. Sci.*, 2017, **391**, 449–456.

13 W. Lubitz, E. J. Reijerse and J. Messinger, *Energy Environ. Sci.*, 2008, **1**, 15–31.

14 T. Sharifi, C. Larsen, J. Wang, W. L. Kwong, E. Gracia-Espino, G. Mercier, J. Messinger, T. Wågberg and L. Edman, *Adv. Energy Mater.*, 2016, **6**, 1600738.

15 A. Annamalai, R. Sandström, E. Gracia-Espino, N. Boulanger, J.-F. Boily, I. Mühlbacher, A. Shchukarev and T. Wågberg, *ACS Appl. Mater. Interfaces*, 2018, **10**, 16467–16473.

16 D. Bae, B. Seger, P. C. Vesborg, O. Hansen and I. Chorkendorff, *Chem. Soc. Rev.*, 2017, **46**, 1933–1954.

17 D. G. Nocera, *Acc. Chem. Res.*, 2012, **45**, 767–776.

18 J. Barber, *Sustainable Energy Fuels*, 2018, **2**, 927–935.

19 X. Cheng, Y. Zhang, H. Hu, M. Shang and Y. Bi, *Nanoscale*, 2018, **10**, 3644–3649.

20 S. K. Matta, C. Zhang, Y. Jiao, A. O'Mullane and A. Du, *Nanoscale*, 2018, **10**, 6369–6374.

21 E. L. Warren, J. R. McKone, H. A. Atwater, H. B. Gray and N. S. Lewis, *Energy Environ. Sci.*, 2012, **5**, 9653–9661.

22 S. W. Boettcher, E. L. Warren, M. C. Putnam, E. A. Santori, D. Turner-Evans, M. D. Kelzenberg, M. G. Walter, J. R. McKone, B. S. Brunschwig and H. A. Atwater, *J. Am. Chem. Soc.*, 2011, **133**, 1216–1219.

23 X. Wang, K.-Q. Peng, Y. Hu, F.-Q. Zhang, B. Hu, L. Li, M. Wang, X.-M. Meng and S.-T. Lee, *Nano Lett.*, 2013, **14**, 18–23.

24 K.-Q. Peng, X. Wang, L. Li, Y. Hu and S.-T. Lee, *Nano Today*, 2013, **8**, 75–97.

25 A. Sartori, M. Orlandi, S. Berardi, A. Mazzi, N. Bazzanella, S. Caramori, R. Boaretto, M. Natali, R. Fernandes and N. Patel, *Electrochim. Acta*, 2018, **271**, 472–480.

26 H. Meng, K. Fan, J. Low and J. Yu, *Dalton Trans.*, 2016, **45**, 13717–13725.

27 M. J. Kenney, M. Gong, Y. Li, J. Z. Wu, J. Feng, M. Lanza and H. Dai, *Science*, 2013, **342**, 836–840.

28 Z. Chen, G. Ma, Z. Chen, Y. Zhang, Z. Zhang, J. Gao, Q. Meng, M. Yuan, X. Wang and J.-M. Liu, *Appl. Surf. Sci.*, 2017, **396**, 609–615.

29 S. W. Boettcher, J. M. Spurgeon, M. C. Putnam, E. L. Warren, D. B. Turner-Evans, M. D. Kelzenberg, J. R. Maiolo, H. A. Atwater and N. S. Lewis, *Science*, 2010, **327**, 185–187.

30 C. Liu, N. P. Dasgupta and P. Yang, *Chem. Mater.*, 2013, **26**, 415–422.

31 K. Sun, S. Shen, Y. Liang, P. E. Burrows, S. S. Mao and D. Wang, *Chem. Rev.*, 2014, **114**, 8662–8719.

32 E. L. Warren, H. A. Atwater and N. S. Lewis, *J. Phys. Chem. C*, 2013, **118**, 747–759.

33 H. Zhang, Q. Ding, D. He, H. Liu, W. Liu, Z. Li, B. Yang, X. Zhang, L. Lei and S. Jin, *Energy Environ. Sci.*, 2016, **9**, 3113–3119.

34 Y. J. Hwang, A. Boukai and P. Yang, *Nano Lett.*, 2008, **9**, 410–415.

35 M. R. Shaner, S. Hu, K. Sun and N. S. Lewis, *Energy Environ. Sci.*, 2015, **8**, 203–207.

36 S. Ida, K. Kearney, T. Futagami, H. Hagiwara, T. Sakai, M. Watanabe, A. Rockett and T. Ishihara, *Sustainable Energy Fuels*, 2017, **1**, 280–287.

37 Y. Yu, Z. Zhang, X. Yin, A. Kvit, Q. Liao, Z. Kang, X. Yan, Y. Zhang and X. Wang, *Nat. Energy*, 2017, **2**, 17045.

38 Y. W. Chen, J. D. Prange, S. Dühnen, Y. Park, M. Gunji, C. E. Chidsey and P. C. McIntyre, *Nat. Mater.*, 2011, **10**, 539.

39 M. T. McDowell, M. F. Lichterman, A. I. Carim, R. Liu, S. Hu, B. S. Brunschwig and N. S. Lewis, *ACS Appl. Mater. Interfaces*, 2015, **7**, 15189–15199.

40 S. Hu, M. R. Shaner, J. A. Beardslee, M. Lichterman, B. S. Brunschwig and N. S. Lewis, *Science*, 2014, **344**, 1005–1009.

41 J. Yu, X. Zhao and Q. Zhao, *Thin Solid Films*, 2000, **379**, 7–14.

42 S.-Y. Lien, D.-S. Wuu, W.-C. Yeh and J.-C. Liu, *Sol. Energy Mater. Sol. Cells*, 2006, **90**, 2710–2719.

43 J. R. McKone, E. L. Warren, M. J. Bierman, S. W. Boettcher, B. S. Brunschwig, N. S. Lewis and H. B. Gray, *Energy Environ. Sci.*, 2011, **4**, 3573–3583.

44 K. Sun, N. Park, Z. Sun, J. Zhou, J. Wang, X. Pang, S. Shen, S. Y. Noh, Y. Jing and S. Jin, *Energy Environ. Sci.*, 2012, **5**, 7872–7877.

45 W. Zhen, X. Ning, B. Yang, Y. Wu, Z. Li and G. Lu, *Appl. Catal., B*, 2018, **221**, 243–257.

46 J.-Y. Jung, J.-Y. Yu and J.-H. Lee, *ACS Appl. Mater. Interfaces*, 2018, **10**, 7955–7962.

47 M. A. Melo, S. A. Carminati, J. Bettini and A. F. Nogueira, *Sustainable Energy Fuels*, 2018, **2**, 958–967.

48 T. K. Townsend, N. D. Browning and F. E. Osterloh, *Energy Environ. Sci.*, 2012, **5**, 9543–9550.

49 C.-Y. Lin, Y.-H. Lai, D. Mersch and E. Reisner, *Chem. Sci.*, 2012, **3**, 3482–3487.

50 K. Peng, Y. Xu, Y. Wu, Y. Yan, S. T. Lee and J. Zhu, *Small*, 2005, **1**, 1062–1067.

51 K. Q. Peng, Y. J. Yan, S. P. Gao and J. Zhu, *Adv. Mater.*, 2002, **14**, 1164–1167.

52 K. Q. Peng and S. T. Lee, *Adv. Mater.*, 2011, **23**, 198–215.

53 A. Kargar, J. Khamwannah, C. H. Liu, N. Park, D. Wang, S. A. Dayeh and S. Jin, *Nano Energy*, 2016, **19**, 289–296.

54 K. Han, T. Kreuger, B. Mei and G. Mul, *ACS Catal.*, 2017, **7**, 1610–1614.

55 A. Annamalai, A. Subramanian, U. Kang, H. Park, S. H. Choi and J. S. Jang, *J. Phys. Chem. C*, 2015, **119**, 3810–3817.

56 Y. Zhao, N. Anderson, K. Zhu, J. Aguiar, J. Seabold, J. V. D. Lagemaat, H. Branz, N. Neale and J. Oh, *Nano Lett.*, 2015, **15**, 2517–2525.

57 A. W. Bott, *Curr. Sep.*, 1998, **17**, 87–92.

58 A. J. Bard, *J. Phys. Chem.*, 1982, **86**, 172–177.

59 H. Gerischer, *Surf. Sci.*, 1969, **18**, 97–122.

60 K. Rajeshwar, *Encycl. Electrochem.*, 2007, **6**, 1–53.

61 W. Gomes and F. Cardon, *Prog. Surf. Sci.*, 1982, **12**, 155–215.

62 W. Schmickler and E. Santos, *Interfacial electrochemistry*, Springer Science & Business Media, 2010.

63 M. Rovezzi and P. Glatzel, *Semicond. Sci. Technol.*, 2014, **29**, 023002.

64 L. Amidani, A. Naldoni, M. Malvestuto, M. Marelli, P. Glatzel, V. Dal Santo and F. Boscherini, *Angew. Chem., Int. Ed.*, 2015, **54**, 5413–5416.

65 G. A. WlvcnuNls, *Am. Mineral.*, 1987, **72**, 89–101.

66 F. Farges, G. E. Brown and J. Rehr, *Phys. Rev. B: Solid State*, 1997, **56**, 1809.

67 R. Asahi, Y. Taga, W. Mannstadt and A. J. Freeman, *Phys. Rev. B: Condens. Matter Mater. Phys.*, 2000, **61**, 7459.

68 G. Fronzoni, R. De Francesco, M. Stener and M. Causa, *J. Phys. Chem. B*, 2006, **110**, 9899–9907.

69 D. M. Pickup, E. A. A. Neel, R. M. Moss, K. M. Wetherall, P. Guerry, M. E. Smith, J. C. Knowles and R. J. Newport, *J. Mater. Sci.: Mater. Med.*, 2008, **19**, 1681–1685.

70 W. B. Kim and J. S. Lee, *J. Catal.*, 1999, **185**, 307–313.

71 V. Luca, *J. Phys. Chem. C*, 2009, **113**, 6367–6380.

72 V. Luca, S. Djajanti and R. F. Howe, *J. Phys. Chem. B*, 1998, **102**, 10650–10657.

73 K. Mase, M. Yoneda, Y. Yamada and S. Fukuzumi, *Nat. Commun.*, 2016, **7**, 11470.